Hydrothermal and magmatic reservoirs at Lazufre volcanic area, revealed by a high-resolution seismic noise tomography

Zack Spica [a,*], Denis Legrand [a], Arturo Iglesias [a], Thomas R. Walter [b], Sebastian Heimann [b], Torsten Dahm [b], Jean-Luc Froger [c], Dominique Rémy [d], Sylvain Bonvalot [d], Michael West [e], Mario Pardo [f]

[a] Instituto de Geofísica, Universidad Nacional Autónoma de México, Av. Universidad 3000, Coyoacán, CP 04510, México DF, Mexico
[b] GeoForschungsZentrum (GFZ), Potsdam, Germany
[c] LMV/UMR6524 (UBP-CNRS-IRD), Observatoire de Physique du Globe de Clermont-Ferrand, Université B. Pascal, Clermont-Ferrand, France
[d] GET/UMR5563 (CNRS-UPS-IRD-CNES), Observatoire Midi-Pyrénées, Toulouse, France
[e] Geophysical Institute, University of Alaska Fairbanks (UAF), United States
[f] Departamento de Geofísica, Universidad de Chile, Chile

A B S T R A C T

We determine here for the first time the geometry and location of the hydrothermal and magmatic reservoirs in the Lazufre volcanic area. This furthers the understanding of the origin of one of the largest worldwide volcanic uplift regions, both in space and amplitude. The exact locations and shapes of the sources generating a double-wide uplift region in the Lazufre found by past deformation data (InSAR and GPS) and generating hydrothermal and magmatic fluids found by geochemical gas analysis have not been well-delimited. In this study, we use seismological data to perform a 3-D high-resolution S-wave velocity model, which allows defining better the locations and shapes of the sources of the deformations and the hydrothermal and magmatic reservoirs. We find three anomalies. Two of them (with S-wave velocity of about 1.2–1.8 km/s) are located below the Lastarria volcano. The shallow one (<1 km below the volcano base) has a funnel-like shape. The deeper one is located between a depth of 3 and 6 km below the volcano base. Both are strongly elliptical in an EW direction and separated by a 2–3 km thick zone with Vs of ~1.5–2 km/s. As far as these anomalies are located under the hydrothermal activity of Lastarria volcano, they are interpreted as a double hydrothermal (the shallow part) and magmatic source (the deeper part). The latter can feed the former. This double hydrothermal and magmatic source is in agreement with previous geochemical, deformation (GPS and InSAR) and magneto-telluric studies. In particular, it explains the double origin of the gases (hydrothermal and magmatic). The third low-velocity zone (with S-wave velocity of about 2.3 km/s) located at 5 km depth and deeper is centered beneath an area of surface uplift as determined by InSAR data. We compare the seismic tomography and InSAR results to propose that this low-velocity zone is at the top of a large reservoir, hosting hydrothermal fluids and possibly also magma.

© 2015 The Authors. Published by Elsevier B.V. This is an open access article under the CC BY license (http://creativecommons.org/licenses/by/4.0/).

1. Introduction

Knowledge of volcanic-reservoir geometry, location and strength is of major importance in monitoring and understanding volcanic unrest. Volcanic reservoirs include magmatic and hydrothermal storage zones and may feed volcanic eruptions when molten material and/or gases reach the surface or a secondary magma reservoir. The depth of a magma reservoir is controlled by a complex association of factors such as the regional stress regime, the magma density, viscosity, volatile content, crystal content or the local crustal structure. In extensional, transtensional, transpressional or strike-slip contexts, the magma reservoirs are generally shallow (between the sub-surface and about 5 km depth) whereas in compressional settings, the magma reservoirs are found to be deeper, without shallow magma reservoirs (e.g., Pritchard and Simons, 2004; Chaussard and Amelung, 2012). These factors also influence the behavior of a volcanic eruption since they control the pressure–temperature condition of the magma reservoir (Dzurisin, 2006; Chaussard and Amelung, 2012). Hence it is important to know if andesitic volcanoes can have shallow reservoirs and we take the Lastarria volcano as a study example.

Direct and convincing seismic images of the geometry and properties of volcano reservoirs are rare (Marsh, 2000). This is due to the fact that traditional seismic tomography, based on earthquake data, is not adequate for obtaining high resolution images of the shallow crust where small magma chambers, dykes or sills are expected (e.g., Lees, 2007). It is particularly true when the number of earthquakes used is small or when the seismograms are difficult to read due to strong path/site effects.

The problem of having a fewer earthquakes can be easily solved with another technique: the ambient seismic-noise tomography (ANT). The ANT technique can produce high-resolution images of the upper crust (e.g., Shapiro et al., 2005), without earthquakes. The technique allows the retrieval of Green's function between pairs of seismometers by cross-correlating the ambient noise recorded at each of them (Shapiro and Campillo, 2004). ANT techniques have successfully been applied to reveal different geological structures at global, regional and local scales using only a few hours to a few months of continuous seismic noise (e.g., Shapiro et al., 2005; Brenguier et al., 2007; Bensen et al., 2007; Mordret et al., 2013). This technique has also been successfully applied to obtain images of volcanic structures, being especially promising for imaging volcano reservoirs at unprecedented resolution, for instance at: the Piton de la Fournaise volcano (Reunion Island; Brenguier et al., 2007; Mordret et al., 2014), the Okmok volcano (Alaska, U.S.A; Masterlark et al., 2010), the Toba volcano (Sumatra, Indonesia; e.g., Jaxybulatov et al., 2014), the Uturuncu volcano (Bolivia; Jay et al., 2012), Mount Asama (Japan; Nagaoka et al., 2012) and at the Colima Volcano (Mexico; Spica et al., 2014).

The Lazufre (an acronym for Lastarria and Cordón del Azufre) area (Pritchard and Simons, 2002) is one of the largest uplift deformation areas in the world (Ruch et al., 2008), located in the Altiplano–Puna Plateau in the central Andes (Chile–Argentina). An area of ∼2000 km^2 started inflating between 1997 and 2000 (Pritchard and Simons, 2002; Froger et al., 2007; Ruch et al., 2009) related to an over-pressurized source at depth. Basaltic volcanoes generally show such uplifts before eruptions (e.g., Wicks et al., 2002; Lu et al., 2010), but it is not clear it is the case for andesitic volcanoes (Pritchard and Simons, 2004; Fournier et al., 2010; Chaussard and Amelung, 2012). A few questions are still unsolved. Geodetic data showed the existence of two sources of deformation (a shallow one and a deep one), but with inaccurate shape and location. The depth of the deep source is not well constrained since it is modeled somewhere between 7 and 18 km (Pritchard and Simons, 2004; Froger et al., 2007; Ruch et al., 2008; Anderssohn et al., 2009; Henderson and Pritchard, 2013; Pearse and Lundgren, 2013) and re-estimated to be between 2 and 14 km by Remy et al. (2014). Hence, the depth of this source may be between 2 and 18 km. These errors are due to the trade-off between the pressure, the shape of the source and the depth. The shallower source was supposed to be unique, at a depth of about 1 km and located just beneath the Lastarria volcano (Froger et al., 2007; Ruch et al., 2009). We show in this study that this source double. Furthermore, these geodetic data cannot discriminate between a hydrothermal and a magmatic system below the Lastarria volcano, as is suggested by geochemical studies.

In this study, we perform a high-resolution 3-D ANT, using data from 26 mainly broadband seismic stations recorded at two different seismic networks deployed at Lazufre. The location and geometry of hydrothermal and magmatic reservoirs below the Lazufre volcanic area are deduced through S-wave velocity tomographic images obtained from the ANT. Results are compared to source inversions from InSAR and GPS data (Pritchard and Simons, 2002, 2004; Froger et al., 2007; Ruch et al., 2008, 2009; Anderssohn et al., 2009; Pearse and Lungren 2013; Remy et al., 2014). As the geometry and the depth of the sources of these deformations cannot be well and uniquely determined with only the InSAR and GPS deformation field, it is important to image these sources with independent data, such as seismicity.

2. Data and methods

2.1. Data

The data used in this study come from two temporary seismic networks installed during two distinct time periods. Network 1 (red triangles in Fig. 1) was deployed from 1 February to 26 March 2008 by the GFZ (Germany) and the DGF (Chile). It was composed of 18 seismometers: 17 broadband (12 Guralp CMG3ESP -60 s- and five Trillium T40 -40 s-) and one short period (LE-3D -1 s-), covering the main deformation zone at Lazufre. Network 2 (blue triangles in Fig. 1) was deployed from November 2011 to March 2013 by the University of Alaska Fairbanks in the framework of the PLUTONS project, but we used only the data from January to March 2012 for this network. Network 2 was composed of eight broadband seismometers (six CMG3T -120 s- and two CMG6TD -30 s-). All seismometers (Fig. 1) were GPS-time synchronized.

The next paragraphs describe the procedures of how the Rayleigh-wave group velocities were obtained from continuous seismic noise records in order to perform an S-wave tomography later.

2.2. Reconstruction of Green's functions from seismic noise

The following steps were applied on the vertical components of each individual continuous seismic data: (1) a removal of the mean and the trend of the signal; (2) a down-sampling to 20 Hz; (3) an instrumental response correction; (4) a 1–30 s band-pass filter; (5) a temporal (1-bit) normalization; and (6) a spectral (whitening) normalization. Steps (5) and (6) were applied in order to diminish the influence of earthquakes and/or non-stationary noise sources at the vicinity of the seismometer. These normalizations allowed using a larger frequency band (e.g., Bensen et al., 2007) and diminishing the influence of heterogeneous distribution of noise sources. Then, cross-correlation functions (CCFs) were calculated for the vertical components of all concomitant station pairs (181) on 200 s time windows. The duration of 200 s was chosen because we found that if a particular station would have a punctual instrumental failure, only a 200 s time window of signal would have been lost. We then stacked all available 200 s CCFs for a given station-pair and added the positive and negative parts of the CCF to enhance the signal-to-noise ratio and to reduce the effect of the heterogeneous distribution of the sources (e.g., Sabra et al., 2005; Bensen et al., 2007). Each folded and stacked CCF converged towards the estimated Green's function (EGF) between each pair of seismometers. Only the EGFs with a signal-to-noise ratio greater than 8 (value that has been found to give the best associated dispersive curves) were used for further analysis. The signal-to-noise ratio was calculated as the ratio of the maximum amplitude of the signal over the root-mean square of the noisy part of the EGF. Since only the vertical components of the ground motion were used in this study, the EGFs are dominated by Rayleigh surface waves. The Love waves were harder to extract from the seismic noise analysis than the Rayleigh waves at Lastarria volcano, so we performed the following analysis using only the Rayleigh waves. Fig. 2 depicts some examples of EGFs with respect to station LGG01 for different azimuths corresponding to different stations.

2.3. Group velocity measurements

The Rayleigh-wave fundamental mode dispersion curves were determined from each EGF via a frequency–time analysis (FTAN;
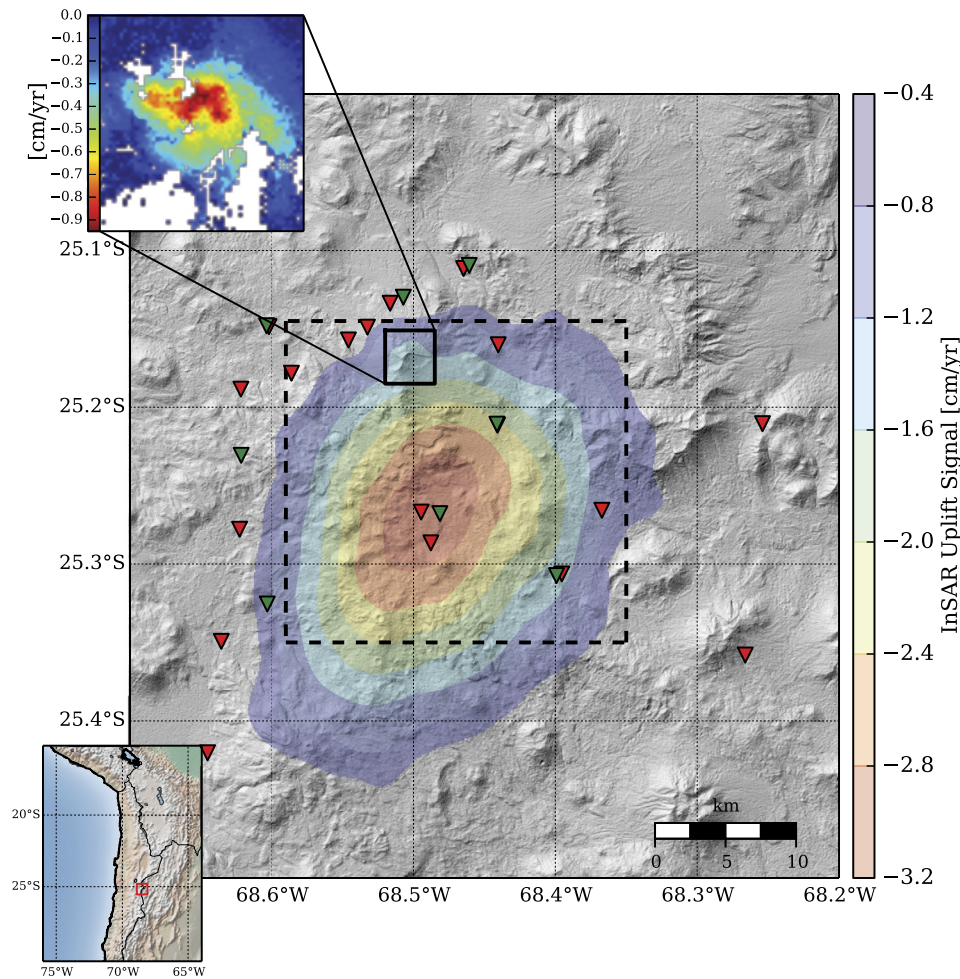
Fig. 1. SRTM-based shaded relief map of the Lazufre volcanic area along with the deformation area (from Froger et al., 2007) and the location of seismic stations sites. Red and blue reversed triangles are the seismic station from network I and network II, respectively (see text for details). Upper corner left: InSAR signal on Lastarria (from Froger et al., 2007) volcano is referred with the plain line rectangle on the map. The dashed-line-square is the contour of the satisfactory-resolution-box. (For interpretation of the references to color in this figure legend, the reader is referred to the web version of this article.)

e.g., Dziewonski et al., 1969). The FTAN technique consists of the application of a set of Gaussian filters with different central frequencies to the input signal spectrum. The group arrival times are estimated from the maxima of the time envelopes. It is known that the method leads to a systematic error in the group velocity estimates due to variations in the spectral amplitudes that cause a shift of the central frequency towards the origin of the filtered spectrum (Levshin et al., 1989). This effect was corrected by computing the centroid frequency (Shapiro and Singh, 1999), which is the frequency where the filtered spectrum reaches its maximum. The resulting dispersion curves were manually selected, i.e., we kept these that vary smoothly in their period, and these for which the stations are separated by at least two wavelengths (Brenguier et al., 2007). The maximum number of 128 ray paths was reached at a period of 4 s. Fig. 2(C) gives examples of dispersion curves for the same ray paths presented in Fig. 2(B), where the main energy is between 1 and 8 s. Fig. 2(C) shows that the paths between pairs of stations at the vicinity of the Lastarria volcano have slower group velocities than those which do not cross the volcano area. This characteristic is well represented in Fig. 3 where the variation of the group velocities around their mean for each path is shown. Fig. 3(B) shows the propagation of the maximum of the envelope of the Rayleigh waves for each selected station pair as a function of interstation distance for frequencies filtered around 3 s. We find that the propagation of the Rayleigh wave packets has a different speed depending on the path. The paths passing close to the

Northern area of the Lazufre volcanic zone and the Lastarria volcano have a Rayleigh wave train traveling with a velocity of about 1.5 km/s whereas the paths passing far from the volcano (mainly located at the Southern area of the Lazufre Volcanic Zone) have a higher velocity of about 2.1 km/s.

2.4. Selection of the dispersive curves

Three quality criteria have been applied in order to select the best dispersive curves: (1) selection of the best EGFs with a signal-to-noise ratio greater than 8; (2) separation of the stations by at least two wavelengths; and (3) clearness and continuity of the Rayleigh wave dispersion curves. Points (1) and (2) are done automatically whereas point (3) is done manually.

The maximum difference in the group velocity between similar inter-station paths (pairs LGG06–LGG18 and LZAE–LZAZ) is about 0.05 km/s, which can be considered as a good proxy for the estimation of the error done on the group velocity between the two networks.

2.5. Tomographic inversion

Rayleigh-wave group velocity tomographic maps were obtained from the picked travel times at different selected periods (1 to 8 s with a step of 0.2 s) by means of a non-linear iterative 2-D tomographic technique (Rawlinson et al., 2008). At each iteration,
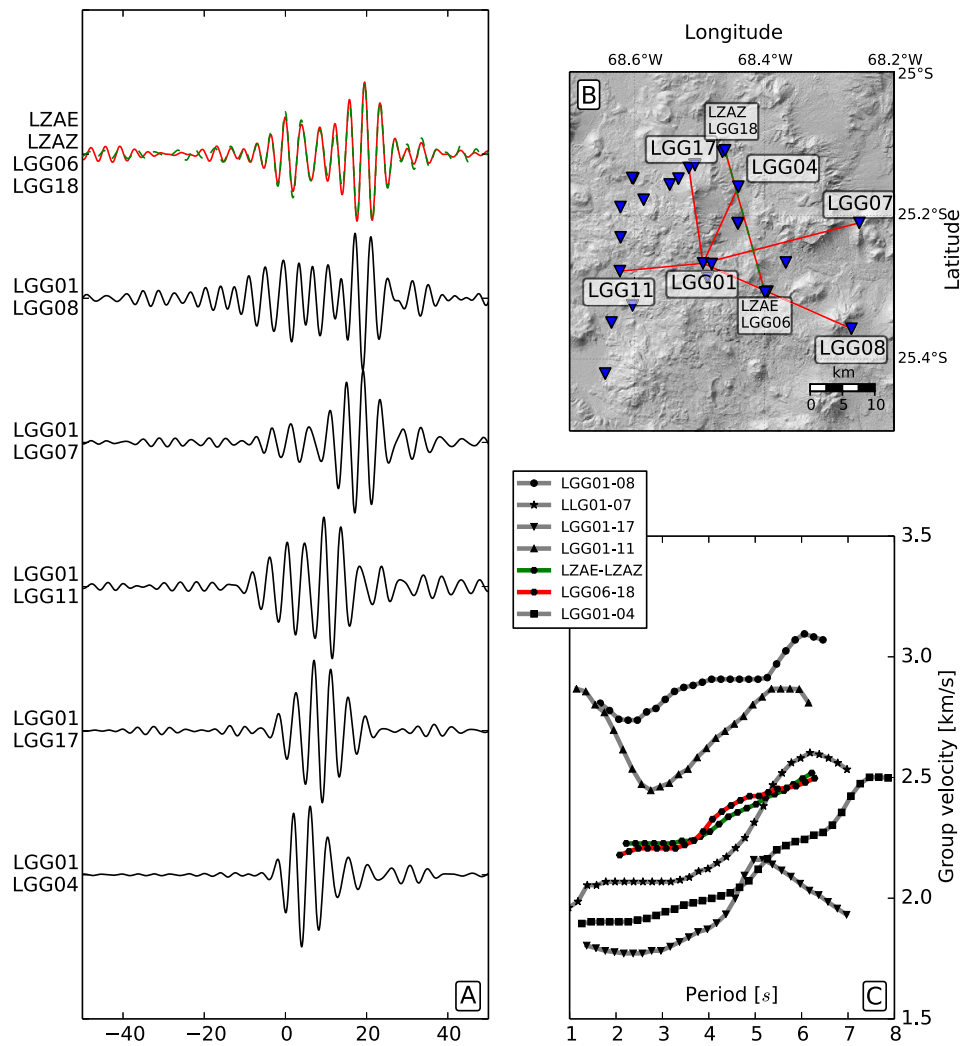
Fig. 2. (A) Examples of EGFs filtered around 4 s for the paths presented in (B). EGFs for station pairs LZAE–LZAZ and LGG06–LGG18 are superposed (red and green) since they cross the same path represented by the red–green line in (B). (B) Map of the Lazufre volcanic zone and seismic station used in this study (reversed blue triangles). The red lines and the red–green line are the paths probed by measurements presented in (A) and (C). (C) Dispersions curves associated to the EGFs presented in (A). The maximum group velocity discrepancy observed between pairs LZAE–LZAZ and LGG06–LGG17 is equal to 0.05 km/s. (For interpretation of the references to color in this figure legend, the reader is referred to the web version of this article.)
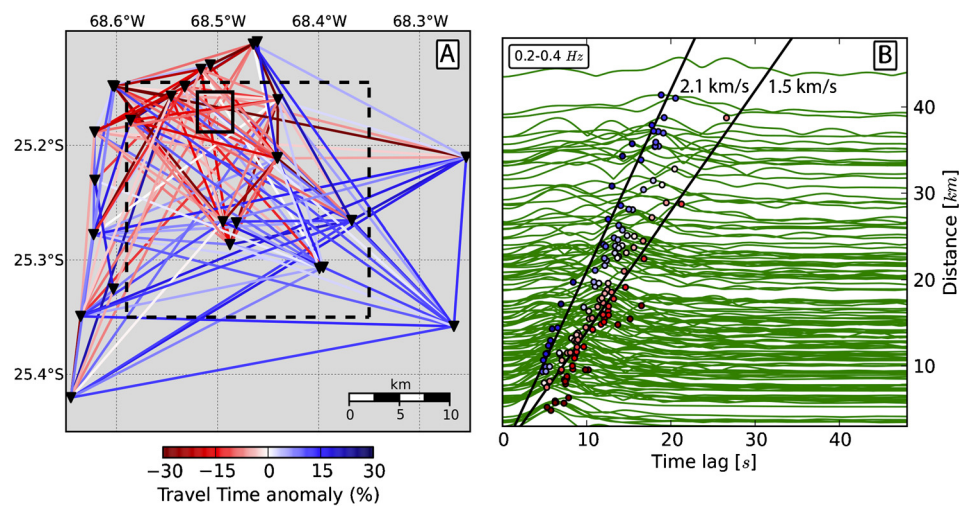
Fig. 3. (A) Ray paths used in this study for the inversion along with the perturbations in travel times with respect to the average velocity observed at 3 s. (B) Envelopes of the ANT cross-correlations at 3 s for Rayleigh waves, plotted as a function of time and interstation distance, the distance between each station pair. The peak of each envelope is shown as a colored circle whose colors refer to the velocity anomaly presented in (A). The plain line rectangle referred Lastarria's deformation. The dashed-line-square is the contour of the satisfactory-resolution-box.
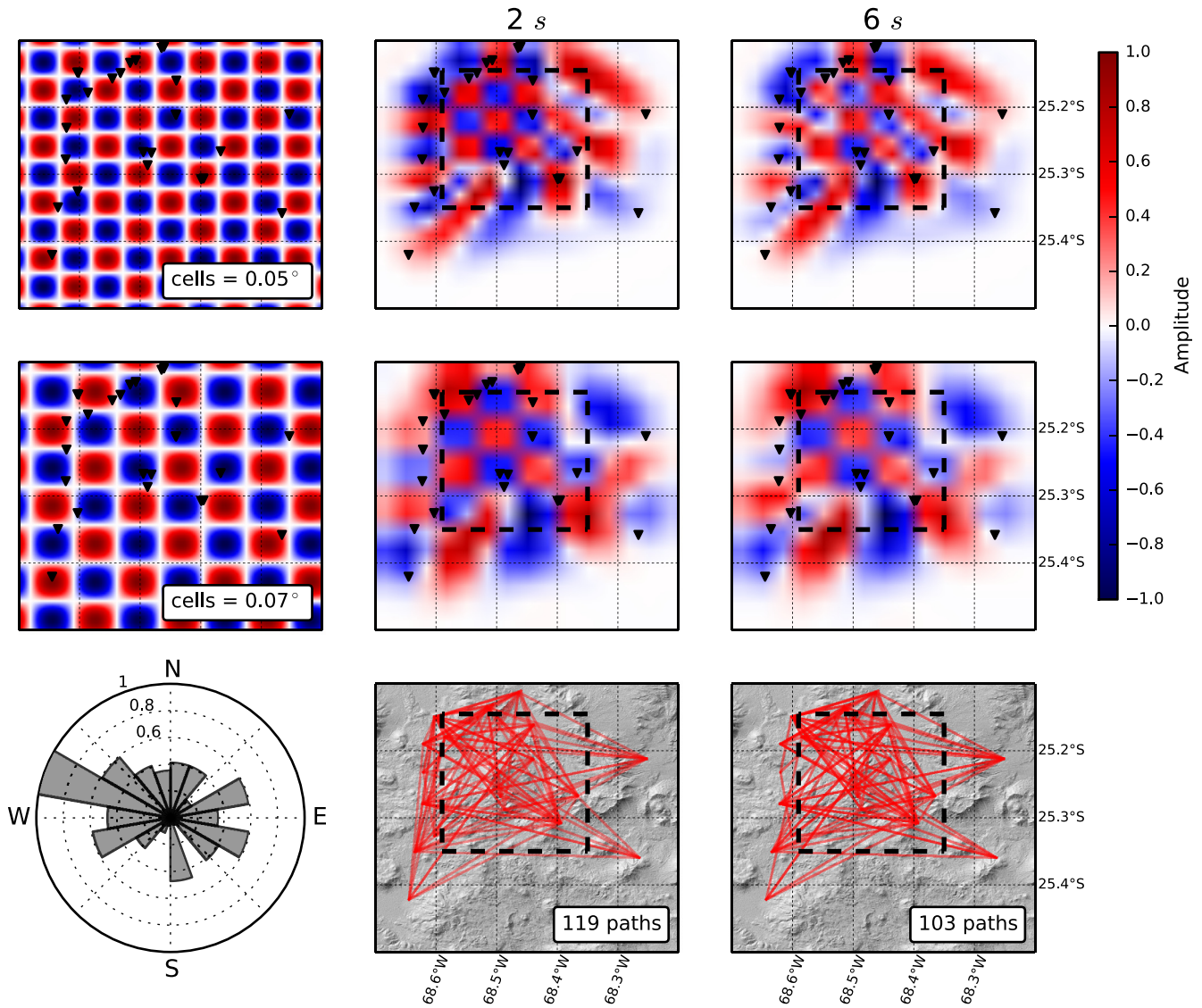
Fig. 4. Resolution analysis of the tomographic inversion. The two first rows are the checkerboard tests showing the resolving capabilities of the inversion. On the left hand are two artificial input models, and the corresponding inversion results are shown for 2 and 6 s period. Resolution of the 2-D tomographic inversion is also assessed through the ray-path density presented on the third raw for 2 and 6 s period. The low left hand corner polar diagram depicts the normalized path density versus the azimuth at 4 s, where the maximum of 128 ray paths is reached. The dashed-line-squares are the contour of the satisfactory-resolution-box.

the ray paths between stations were updated so that the influence of their length was taken into account to compute theoretical arrival times. This step was carried out by the Fast Marching Method (FMM) (Sethian, 1996; Rawlinson and Sambridge, 2004). The FMM is a grid-based Eikonal solver that uses implicit wavefront construction and provides stable and robust solutions for wave propagation in highly heterogeneous media (e.g., Rawlinson and Sambridge, 2004; Rawlinson et al., 2008), as it is expected for volcanic environments. The inversion method then seeks for the perturbation of the model parameters that best match the group velocity. Once the perturbations are estimated, the model is updated and the propagation paths are retraced using the FMM scheme. The Fast Marching Surface (wave) Tomography (FMST) code was used in this study (cf. Rawlinson et al., 2008). The tomographic inversion was performed on a 0.016° by 0.016° (∼1.8 km by ∼1.8 km) grid at each period, which gave an optimum balance between resolution and recovery. As we perform here a 2-D tomography with respect to the period, we have no direct information on the depth. The depth resolution will be discussed in the next paragraph, while performing a 3-D inversion. The weight of the spatial smooth-

ing and damping was estimated using standard L-curve analysis (e.g., Menke, 2012). The inversions were carried out with a starting model of constant velocity equal to the mean group velocity observed at each period. More specifically, the mean group velocity was chosen as the average of all the group velocities calculated using the FTAN method for every existing pair of stations for a given period. Synthetic checkerboard tests were performed in order to investigate the resolution of our results at different periods (Fig. 4). Each checker model was assigned with alternating velocity perturbations of ±0.5 km/s. A "satisfactory-resolution-box" was then defined where the results can be interpreted with fair enough robustness (represented in Figs. 1, 3, 4 and 5). The box excludes the areas of the model, where the smearing of the checkerboards is evident at all periods. Resolution of the 2-D tomographic inversions is also assessed through the ray-path density as presented in Fig. 4.

2.6. Three-dimension shear-wave velocity model

First, we generated a one-dimensional velocity model. To accomplish this, "local" dispersion curves were constructed at each cell inside the satisfactory-resolution-box from the Rayleigh group
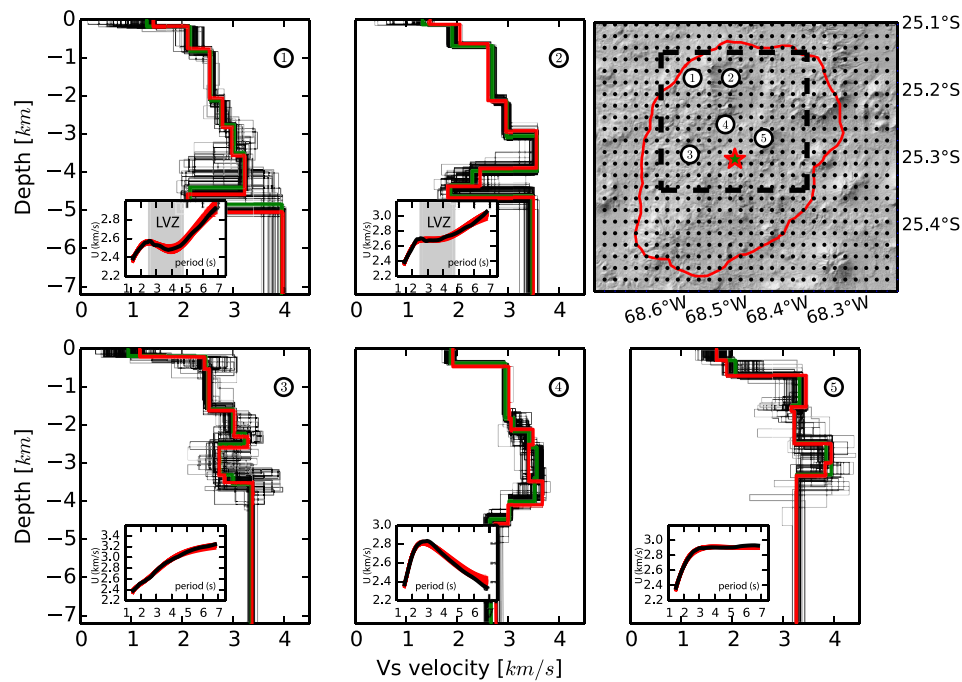
Fig. 5. Selected examples for the Vs versus depth inversion and their location at Lazufre. 1-D velocity models are referred with a number that is reported on the map. Black lines are the 200 best models. Green lines are the averaged velocity model for the 200 best models obtained. The red lines are the last iteration's model (best misfit). Black dots on the map indicate inversion nodes used to obtain the 3-D shear wave velocity model described in the text and presented in Figs. 6 and 7. The dashed-line-square is the contour of the satisfactory-resolution-box. The green star represents the center of the main InSAR anomaly and the red contour line represents the shape of the main InSAR anomaly. (For interpretation of the references to color in this figure legend, the reader is referred to the web version of this article.)

velocity tomographic maps obtained at each of the previously mentioned periods. These curves were fit by polynomial functions and then inverted using a simulated annealing algorithm that minimizes the misfit value calculated as the semblance between the data (the local dispersion curve) and the synthetics (Iglesias et al., 2001). The inversion was performed for thickness and S-wave velocity of eight layers overlying a half-space. The initial model at each cell was taken as the last output model of the previous inverted cell, providing a natural smoothing for the entire model. Finally, the 200 best models were averaged to produce a "local" 1-D S-wave velocity structure versus depth at each cell. All of the synthetic dispersion curves show a good fit to the observations (the local dispersion curve) with low mean value (0.11 km/s) of the misfit for all inversions. Examples of 1-D S-wave velocity models for selected cells are presented in Fig. 5.

Second, a model showing a 3-D distribution of shear-wave velocities was generated from the inverted 1-D models for all the 195 cells (Fig. 6, Fig. 7). This model was constructed using a smooth bivariate spline approximation of three cell length in order to represent the structures smoothly.

Fig. 6 depicts six horizontal slices across the 3-D shear-wave velocity model at different depths (0.4, 1, 2, 4, 5 and 6 km). Fig. 7 shows two vertical profiles crossing the Lastarria volcano (corresponding to A–A′ and B–B′ in Fig. 6(A)) across this model.

3. Results and discussion

All models and inversions are performed in a half space, where the free surface is the mean elevation of 4.3 km above sea level. The depths values are given with respect to this reference level.

3.1. Identification of low velocity anomalies

Three S-wave velocity anomalies have been identified at Lazufre. The first one (A in Fig. 7) has an S-wave velocity of about 1.6 km/s, corresponding to a velocity contrast of 54% with

respect to the surrounding S-wave velocity of about 3.5 km/s (Fig. 7), which is a typical value of crustal rocks. This ultra low velocity zone (ULVZ) A is shallow, between 0 and 1 km depth, and has a funnel-like shape that is larger when close to the surface and smaller at around 1 km depth. Its horizontal extension is slightly larger than the Lastarria volcano edifice, depending on the depths considered (Figs. 6(A) and 6(B)). It has an extent of about 9 km in the EW direction, 4 km in the NS direction and 1 km in the vertical direction, at a depth of 0.4 km (Figs. 6(A) and 6(B)). Considering its funnel-shape and the 1.8 km/s Vs iso-contour (this value corresponds to a 26% melted magma as described after), the volume of this anomaly A is about 12 km^3. The ULVZ A is located just below a region of high fumarolic activity of Lastarria volcano (Naranjo, 1985; Aguilera et al., 2012). The location of the ULVZ A, as well as its particular funnel-shape, strongly suggest the presence of a material rich in fluids, which would decrease the S-wave velocity. Hence, the funnel-like shape of the ULVZ A may be associated with a "classical" hydrothermal model (e.g., Ingebritsen and Sorey, 1985) where a central up-flow zone feeds various superficial hydrothermal features. The lateral outflows are probably regulated by some structural control of the permeability, but the important fracturing, heating and fluid migrations contribute to extend the hydrothermal system near the surface. The presence of fluids in the ULVZ A is also suggested by the hybrid character (combination of low and high frequencies) of many small shallow seismic events, some of them being monochromatic and others having several narrow frequency-peaks. Fig. 8 illustrates an example of a hybrid event with two dominant frequencies and a long duration of more than 20 s, suggesting a persistent resonating phenomenon due to the presence of fluids.

The second anomaly (B in Fig. 7) is also considered as a ULVZ, since it has an S-wave velocity of about 1.3 km/s, corresponding to a velocity contrast of 63% with respect to the surrounding rock velocity. It is the smallest velocity found in the studied region. Anomaly B is located between a 3 and 6 km depth and has an
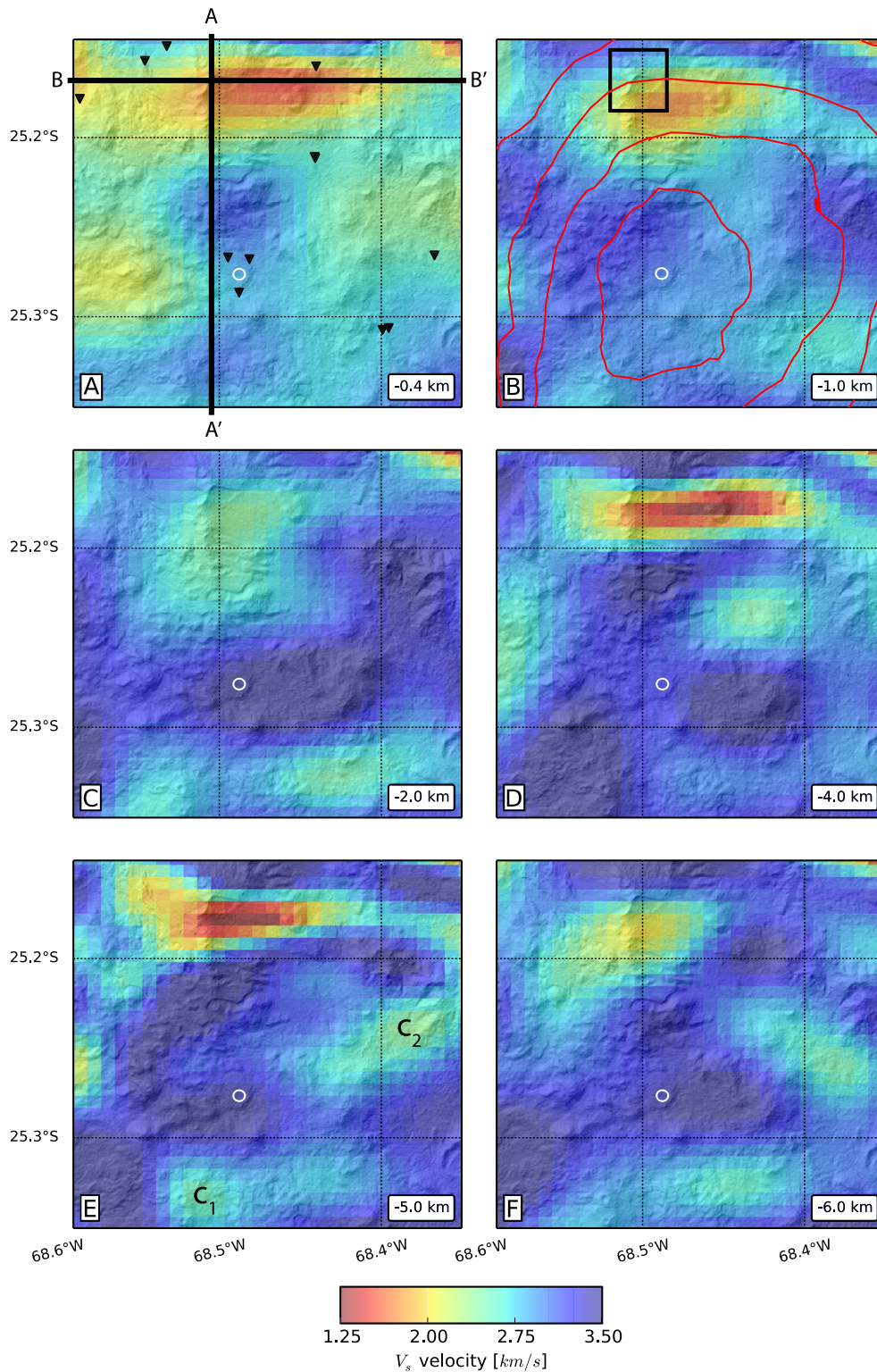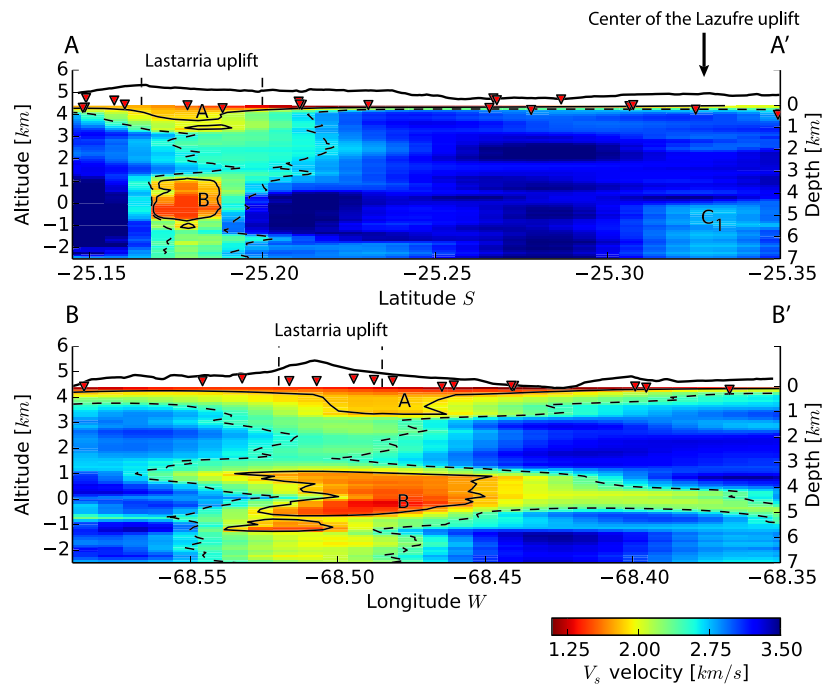
Fig. 6. Horizontal slices through the 3-D Vs-velocity model inside the satisfactory-resolution-box. The black rectangle in (B) depicts the zone affected by the Lastarria uplift. The red lines in (B) represent the Lazufre uplift. The white dots present in all sections refer to the center of InSAR anomaly. Labels associated to velocity anomalies are referred in the text. (For interpretation of the references to color in this figure legend, the reader is referred to the web version of this article.)

oblate spheroidal-shape, elongated in an EW direction, in the same direction as the hydrothermal reservoir A.

Although a detailed characterization of a body cannot be assessed only on its S-wave velocity, we assume that the ULVZ B, which coincides with the active Lastarria volcano, infers high temperatures and/or the presence of partial melting in the shallow crust (e.g., Christensen and Mooney, 1995; Lees, 2007; Masterlark et al., 2010). These high temperatures found on Lastarria (up to 400 °C; Aguilera et al., 2012) may be due to the presence of close magma, at a few kilometers of the surface. We speculate that the ULVZ B is a magma chamber combined with the presence of fluids generated by the partial degassing of this magma from 6 km depth until the surface. As the deepest part of the hydrothermal reservoir A, at 1 km depth, has the same shape as the magma

Fig. 7. Vertical slices through the 3-D Vs-velocity model along the A–A′ and B–B′ profiles represented in Fig. 6(A). Cross-section results are presented with no vertical exaggeration (1:1) along with the topography. The continuous black line represents the 1.8 km/s iso-velocity field and the dashed black line depicts the 2.53 km/s iso-velocity field. The topography is represented here but has not been taken into account in the inversion process. The reference altitude of 4300 m a.s.l. corresponds to the average between the highest at lowest seismometer altitudes. Labels associated to velocity anomalies are referred in the text.
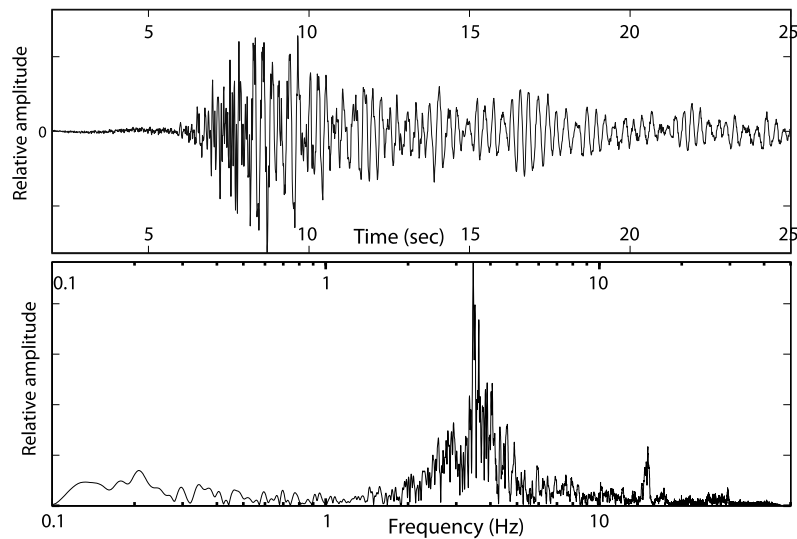

Fig. 8. Example of a hybrid event (6 April 2006) observed at Lastarria volcano and filtered between 1 and 49 Hz recorded on the vertical component of a broadband seismometer (Guralp 40 T). Many of such events are recorded at Lastarria (i.e. more than 100 in a week in April 2006).

reservoir B (Fig. 7) and elongated in the same direction (E–W), we hypothesize that the latter feeds entirely or partly the former located just above. Hence, the magma reservoir B may explain part of the degassing observed in the Lastarria volcano and the presence of the hydrothermal system A located just at the top of it (Fig. 7). Magma chamber B is probably smaller than the one imaged in Fig. 7 because of the smoothing used in the S-wave maps.

Considering a 1.8 km/s Vs iso-contour, the maximum size of anomaly B is 9 km in the E–W direction, 3 km in the N–S direction and 3 km for its vertical extension, consistent with a magma reservoir of 81 km^3. The choice of a contour 1.8 km/s is somehow artificial. In order to estimate the error done on the shapes of the reservoirs, we show two contours in Fig. 7: one corresponding to 1.8 km/s and another one to 2.53 km/s. The choice

of 2.53 km/s corresponds to the smallest velocity for which we found a unique reservoir of S-wave velocities varying from about 1.25 km/s to 2.53 km/s (Fig. 7). Following a theoretical relationship for a fluid-saturated granite at 800 °C and a pressure of 0.1 GPa (corresponding to a depth of 5 km) as a function of porosity filled with different rhyolite melt and water–CO_2 contents, the percentage of melted material is estimated to range between 31% and 26% (Chu et al., 2010). Even though the Vp/Vs ratio is unknown, it can be estimated from the same theoretical relationship. In our case, it is equal to about 2.25. Although these values appear very high, they are similar to the one obtained for the magma reservoir underlying the Yellowstone caldera (Chu et al., 2010). Note that the anomalies A and B are not clearly separated. We have a gradient of S-wave velocity from A to B and not a strong contrast of velocity.
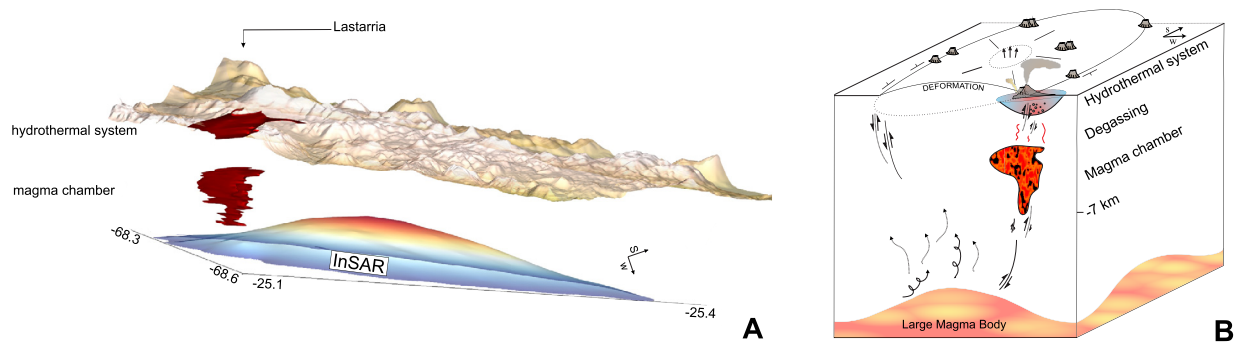
Fig. 9. S-wave velocity anomalies under Lastarria volcano, topography and InSAR deformation (from Froger et al., 2007). (A) 3-D view of the magma chamber and hydrothermal system beneath the topography. Magma chamber and hydrothermal systems are delimited by the 1.8 km/s Vs iso-contour. The blue–red relief represents the InSAR uplift measurements as in Fig. 1. The magma chamber took place at the border of the uplift. Uplift might have produced a circular network of faults facilitating the magma intrusion from a deeper source as explained in (B). (B) Cartoon representation of the volcanic system. Lastarria volcano is near the edge of the InSAR uplift (Froger et al., 2007). The uplifting episodes may have caused a fracture girdle (as at Uturuncu; Walter and Motagh, 2014) which could represent a preferential path-way for magma, resulting in the formation of the magma chamber imaged in this study (LVZ B). Deeper magma body may have feed the actual magma chamber. Deep magma may also cause an important degassing or an alteration of the upper crust (symbolized by the squiggly black arrows), which is may be reflected in our tomography by the LVZ C. The magma chamber's gases feed and warm up the hydrothermal system (symbolized by the red arrows). (For interpretation of the references to color in this figure legend, the reader is referred to the web version of this article.)

The S-wave velocity between A and B is about 1.5–2.0 km/s, much smaller than the 3.5 km/s of the surrounding rock. If we chose a Vs iso-contour of 2.53 km/s instead of 1.8 km/s, we have a single anomaly and not a clear separation between the two anomalies A and B (Fig. 7). Nevertheless, the difference of the two velocities (1.8 and 2.53 km/s) is strong enough to interpret it as due to two different materials, without saying that they are not related. Indeed we think that the anomaly A is related to the anomaly B, in the sense that the degassing in B migrates until the subsurface where fluids concentrate. Both anomalies are related to Lastarria volcano rather than Lazufre, with important implications as further discussed below.

The third low velocity anomaly (C1, C2 in Fig. 6; C1 in Fig. 7) is not as strong as the previous ones. It consists of a patchwork of weak velocity zones with S-wave velocity of about 2.7 km/s, corresponding to a relative velocity contrast of 23% with respect to the surrounding material. This is well observed between a depth of 5 to 7 km, located at the Southeastern part of the Lazufre volcanic zone (denoted by C1 in Fig. 7(A)), beneath the center of the main uplift deformation. As our model does not image features deeper than 7.0 km, the presence of a larger intra-crustal magma reservoir extending to greater depths (Pritchard and Simons, 2002, 2004; Froger et al., 2007; Ruch et al., 2008, 2009; Anderssohn et al., 2009) cannot be dismissed. Nevertheless, we can affirm that a large magma chamber located at depths less than 7 km is not imaged by our tomography under the main deformation anomaly. This information reduces the uncertainties on the depths of such a magma chamber proposed by Remy et al. (2014) and allows us to better estimate the volume of this source (thickness of the flat-topped magma chamber or of the sill). As a consequence, we suggest that this patchwork of low velocity zones may correspond to the upper limit of the deeper large magma reservoir mentioned before. The weak shear-wave velocity observed could result from a strong heating, an important fractured zone and/or a significant concentration of volatile at these depths. A strong degassing may also occur, resulting in a decrease of S-wave velocity.

3.2. Tectonic interpretation

The E–W direction of both reservoirs below Lastarria volcano is near the edge of the Lazufre inflation area. An EW trend is not compatible with the regional stress tensor found by the study of regional fractures, dikes and the interpretation of the InSAR data (Ruch and Walter, 2010). This E–W direction may rather be related

a) to a local stress tensor which may be the superposition of the regional stress tensor modified by the local stress tensor generated by the main deformation anomaly, as observed at other volcanoes (e.g., Legrand et al., 2002) or b) to reactivated pre-existing structures. A large magma chamber deeper than ~7 km depth below the main deformation at Lazufre explains the InSAR data and would generate radial fractures close to the top of this anomaly and circular fracture zones at the margin of this deformation zone, which is typical of a caldera formation. Inflation of a deep reservoir could generate a stress field favoring the generation of the anomaly detected in this study. The position of our anomalies A and B agrees with the location of a girdle of volcanoes encircling Lazufre area (Froger et al., 2007). As far as the Lastarria volcano is located at the border of the main deformation anomaly, as well as other volcanic edifices (Froger et al., 2007), we conjecture that the E–W direction corresponds to an active part of this ring fracture zone around the main anomaly (Fig. 9). Fracture studies will address the hypothesis compatible with a stress transfer model, which may explain geometry and positioning of the anomalies.

3.3. Integration with other studies

Our results are consistent with previous (1) geochemical, (2) geodetic, (3) seismological and (4) magneto-telluric studies at Lastarria but significantly add resolution and interpretation to the reservoir problem.

(1) A coupling of the shallow hydrothermal source to a deeper magmatic source was also deduced by the past geochemical analysis (Aguilera et al., 2012). Effectively, the Lastarria volcano has four intense and continuous fumarolic fields (Naranjo, 1985) with outlet temperature from 80 °C to over 408 °C between 2006 and 2009 (Aguilera et al., 2012), located just above our hydrothermal reservoir A. It corresponds also to the magma reservoir B, where high degassing may exist (Fig. 7) and may explain such high temperatures of about 400 °C that a hydrothermal system alone could not be explained. These superficial fumarolic fields seem to exist at least since the discovery of Lastarria volcano at the end of the 19th century (Aguilera et al., 2012). The fluids emanating close to the volcanic conduit have chemical and isotopic compositions traducing both a magmatic and a hydrothermal source (Aguilera et al., 2012). One shows a main magmatic-source degassing process while the other indicates that the fluids are emanated from a superheated vapor at hydrothermal conditions that is later cooled

and condensed at shallow depth, inhibiting the formation of a continuous aquifer at shallow depth (Aguilera et al., 2012). Our results suggest that a possible magma reservoir is much closer to the surface (located 3–6 km below the surface) than previously assumed by Aguillera et al. (2012). These significant fluid reservoirs may explain why Lastarria volcano is currently the most important gas source in the Chilean central volcanic zone (17°S to 26°S), with a total volatiles output (∼13,500 t/d; Tamburello et al., 2014). The concentrations of HCL and SO_2 of the Lastarria gases found by these authors are too high to be originated at a depth higher of ∼10 km and should come from a shallower magmatic reservoir. Therefore, we interpret the anomaly B as a magmatic reservoir rather than a hydrothermal reservoir only. The presence of such quantities of gases come more likely from shallower depths, such as 3–6 km (our magma reservoir B), inferring a high-temperature open-vent system. The isotopic composition of the fluids also shows a low local precipitation origin, especially in this extremely dry region (Aguilera et al., 2012), confirming its magmatic origin instead of a meteoritic contribution. Hence, we propose that the gasses emitted at the Lastarria volcano and concentrated in the hydrothermal system A (Fig. 7) may originate from the degassing of the magma chamber B (Fig. 7) and not from the more distant (about 13 km) and deeper (7–15 km depth) magma reservoir below the LVZ C. Nevertheless a stress interaction between these different sources is likely, as proposed earlier (Ruch et al., 2009).

(2) The Lazufre's uplift was detected by InSAR measurements and has started sometime between 1997 and 2000 (Pritchard and Simons, 2002, 2004; Henderson and Pritchard, 2013). Today, it has an extent of about 2000 km^2 (Ruch and Walter, 2010; Henderson and Pritchard, 2013; Pearse and Lundgren, 2013; Remy et al., 2014). The maximum ground deformation velocity is about 3.0 cm/yr for the March 2003–May 2010 period (Ruch et al., 2008; Anderssohn et al., 2009; Remy et al., 2014). More recently, Remy et al. (2014) gave an estimation of the maximum uplift rate of 3.85 ± 0.5 cm/yr using GPS data. The precise nature of the process responsible for the observed uplift is still under debate. Several models of deformation sources, based on InSAR and GPS data inversion, have been proposed for the Lazufre. One of the difficulties in modeling the depth and size of these sources is related to the fact that InSAR data only consider one – and not three – directions of the displacement field. The source-depth is particularly difficult to solve because of the classical trade-off between the geometry (sill, ellipse, oblate, prolate), the amplitude of the volume change and the depth itself (Pritchard and Simons, 2004; Froger et al., 2007; Remy et al., 2014; Walter and Motagh, 2014). All aforementioned geodetic studies proposed the presence of an existing magma chamber inflating at depths ranging between 7 and 17 km to explain this large wavelength ground inflation, and they explored a large range of possible source geometries (e.g., spherical, prolate ellipsoid and penny-shaped crack). The source explaining the main deformation zone is at a depth between 10 and 12 km for Pritchard and Simons (2002), between 9 and 17 km for Pritchard and Simons (2004), between 7 and 15 km for Froger et al. (2007), between 8.5 and 13 km for Ruch et al. (2008), between 12 and 14 km for Ruch et al. (2009) and at 10 km for Ruch and Walter (2010) and Anderssohn et al. (2009). All these depths have a reference level of 4 km a.s.l., which is the average altitude of the region. Ruch et al. (2008) and Anderssohn et al. (2009) proposed that the uplift observed during the 2003–2008 period was caused by a fast lateral expansion, up to 8 km/yr of a thin magmatic sill or a more extended reservoir. Nevertheless, Pearse and Lungren (2013) and Remy et al. (2014), using different approaches, showed that the surface displacement measured at Lazufre could

be explained without any need for significant lateral source expansion. Both studies lead to the conclusion that the surface displacements observed at Lazufre are related to a pressure increase in a sill or a large magma chamber located at depth between 2 and 14 km below ground surface. Nevertheless, while these two latter studies have greatly decreased the class of viable magma chamber shapes, the non-uniqueness of the solution using deformation data alone prevents the reduction of large uncertainties on both the shape of the source and its depth. For example, Remy et al. (2014) confirmed the observation by Ruch et al. (2008) that a large flat-topped magma chambers produced almost identical surface displacements to a thin sill. The position of the LVZ C on map views coincides with the center of the main InSAR uplift area (of about 3.0 cm/yr) and also with the deeper magma chamber found by these previous studies. As no ULVZ is detected below the main deformation anomaly between the surface and 7 km depth, this information may help in the modeling of InSAR and GPS data. Our seismic tomography only images the roof of the deep reservoir.

A second and smaller inflation region centered at the Lastarria volcano that started in 2003, has been identified by InSAR data (Froger et al., 2007). The Lastarria is the unique active volcano of the area and is located at the Northwest margin of the Lazufre zone (plain line rectangle in Fig. 1). The deformation has an uplift rate of about 0.9 cm/yr in average, with a maximum rate of 2.5 cm/yr between March 2003 and June 2005, and affects a 6 km wide area (Froger et al., 2007). The depth of a single point source of this deformation has been estimated at about 1 km (Froger et al., 2007) and at 0.6–0.9 km (Ruch and Walter, 2010) below the summit of Lastarria volcano, inside the volcanic edifice, suggesting a hydrothermal origin. The region of the small InSAR uplift of about 1 cm/yr at Lastarria volcano and of about 6 km width (Froger et al., 2007; Remy et al., 2014; Fig. 1) lies inside the LVZ A. The LVZ A is even larger than the deformation field, which is expected since the fluids located at the edges of the hydrothermal system may have a small influence on this InSAR deformation. In contrast, the fluids concentrated at the middle of the hydrothermal system A may contribute with a greater force to this uplift. The pressure increase inside the magma chamber B may also partly explain the Lastarria volcano deformation because it is also located just below the Lastarria volcano uplift. Froger et al. (2007) suggested a source depth at 1 km below the summit of the volcano to explain the Lastarria volcano deformation field. This depth roughly corresponds to the spatial average of the two sources we imaged (A and B), even though we have not shown it. Various modeling of the Lastarria deformation have to be performed to address the respective influences of these S-wave anomalies on Lastarria deformation.

(3) The deeper structure of the Lazufre system has been studied using P-wave travel time delay tomography by Heimann et al. (2013). They find up to 40% P-wave velocity reductions between about 5 and 20 km depth under the Lazufre large-scale inflation area, a result that is compatible with our study. Stacked PS receiver functions from teleseismic and regional earthquakes confirm a strong S-wave velocity contrast in the center of the uplift at a depth of about 9 km (5 km below sea level; Heimann et al., 2013).

(4) Magneto-telluric tomographies performed in a small region around the Lastarria and with a good resolution to a depth of 10 km (Díaz et al., in press), depict very similar features to our results. These authors observed a shallow resistivity anomaly (below 1 Ω m) between 0 and 1.5 km, as well as the existence of an anomaly (below 10 Ω m) to a depth of about 3–6 km oriented in an EW direction, which is in agreement with our ANT results. Both, the seismological and MT tomography, showed that the anomaly (i.e., magma reservoir) is not precisely below the summit but at a few km southward. MT tomography has been performed at a larger

region by Budach et al. (2013) below the main deformation zone, where they found a very large anomaly at depths between 20 and 70 km with offset and dips to the East.

3.4. Comparison with the Uturuncu uplift

Studies have been realized at the Uturuncu uplift, in Bolivia, with a deformation anomaly similar to the Lastarria's one (e.g., Pritchard and Simons, 2002; Jay et al., 2012). ANT performed by Jay et al. (2012) revealed a low-velocity zone at depths between 1.9 and 3.9 km below the center of the crater. These authors suggested that since the LVZ persists at 3.9 km depth, it could represent either the final pathway of ascending magma from greater depths or a zone of hydrothermal alteration. In another study, a large zone of low S-wave velocity of 2.5–2.9 km/s has been identified in the Altiplano–Puna volcanic complex below Uturuncu at depths between 10 and 20 km (Ward et al., 2014). The 3-D tomography performed by these authors revealed a low-velocity zone with a diameter of ∼200 km and a thickness of ∼11 km, interpreted as a magmatic underpinnings associated to the 11–1 Ma ignimbrite flare-up. A deep (below 15 km) low S-wave velocity anomaly has been imaged at Lazufre by Ward et al. (2013). This anomaly is interpreted as belonging to the Southern Puna Magma Body (e.g., Bianchi et al., 2013). Such large body should be seen below the Lazufre volcanic complex, but it has not been imaged in our results because they are limited to the first 7 km. At Uturuncu volcano, a fracture girdle encircling the deformation region was found (Walter and Motagh, 2014) similarly to the volcanic edifices concentrated at the periphery of the Lazufre deformation zone.

4. Conclusion

We show that the Lastarria volcano hosts a shallow (3 to 6 km depth) magma reservoir. This is therefore a new example of andesitic volcano with shallow magmatic chamber in a compressional context (Chaussard and Amelung, 2012). We show that the source of the major uplifts observed at Lastarria volcano and Lazufre area is more complex than the one proposed in past studies (Froger et al., 2007; Ruch et al., 2009; Aguilera et al., 2012). Three low S-wave velocity anomalies have been found at Lazufre. One (region A) is very shallow, between 0 and 1 km depth below the active Lastarria volcano, covering a zone of about 36 km^2 at 0.4 km depth, and is naturally interpreted as a hydrothermal system already identified by previous geochemical and geophysical results. It is slightly larger than the intense and permanent fumarolic zone of the active Lastarria volcano. A second anomaly (region B) has a sill-shape oriented in an E–W direction, between 3 and 6 km depth. Both the depth and the shape of this second anomaly suggest a magmatic reservoir, even if we cannot exclude the presence of some magmatic fluids that are degassing at these depths. A third one, smaller in amplitude, is located under the center of the main deformation anomaly, at depths greater than 5 km. This smaller anomaly may be the upper manifestation of a deeper magmatic chamber that we cannot image with the frequency range of our study. Our results are in very good agreement with past magnetotelluric and earthquake tomographies, geodetic deformations, gas composition and observed temperatures at Lastarria volcano. Our work shows the shallow structure of Lazufre region using seismic records (without earthquakes) to a depth of 7 km. We still require detailed imaging of the deeper structure in this area to infer the depth and the size of a large and deep magma body that generates the Lazufre uplift. The results will help in future works to constrain the sources responsible of InSAR deformation and furnish a velocity model in order to locate earthquakes in the Lazufre area.

References

Aguilera, F., Tassi, F., Darrah, T., Moune, S., Vaselli, O., 2012. Geochemical model of a magmatic–hydrothermal system at the Lastarria volcano, northern Chile. Bull. Volcanol. 74 (1), 119–134. http://dx.doi.org/10.1007/s00445-011-0489-5.

Anderssohn, J., Motagh, M., Walter, T.R., Rosenau, M., Kaufmann, H., Oncken, O., 2009. Surface deformation time series and source modeling for a volcanic complex system based on satellite wide swath and image mode interferometry: the Lazufre system, central Andes. Remote Sens. Environ. 113 (10), 2062–2075. http://dx.doi.org/10.1016/j.rse.2009.05.004.

Bensen, G.D., Ritzwoller, M.H., Barmin, M.P., Levshin, A.L., Lin, F., Moschetti, M.P., Shapiro, N.M., Yang, Y., 2007. Processing seismic ambient noise data to obtain reliable broad-band surface wave dispersion measurements. Geophys. J. Int. 169 (3), 1239–1260. http://dx.doi.org/10.1111/j.1365-246X.2007.03374.x.

Bianchi, M., Heit, B., Jakovlev, A., Yuan, X., Kay, S.M., Sandvol, E., Alonso, R.N., Coira, B., Brown, L., Kind, R., Comte, D., 2013. Teleseismic tomography of the southern Puna plateau in Argentina and adjacent regions. In: Recent Megathrust Earthquakes and Tsunamis: Observations and Processes. Tectonophysics 586, 65–83. http://dx.doi.org/10.1016/j.tecto.2012.11.016.

Brenguier, F., Shapiro, N.M., Campillo, M., Nercessian, A., Ferrazzini, V., 2007. 3-D surface wave tomography of the Piton de la Fournaise volcano using seismic noise correlations. Geophys. Res. Lett. 34 (2), L02305. http://dx.doi.org/10.1029/2006GL028586.

Budach, I., Brasse, H., Díaz, D., 2013. Crustal-scale electrical conductivity anomaly beneath inflating Lazufre volcanic complex, Central Andes. J. South Am. Earth Sci. 42, 144–149. http://dx.doi.org/10.1016/j.jsames.2012.11.002.

Chaussard, E., Amelung, F., 2012. Precursory inflation of shallow magma reservoirs at west Sunda volcanoes detected by InSAR. Geophys. Res. Lett. 39 (21).

Christensen, N.I., Mooney, W.D., 1995. Seismic velocity structure and composition of the continental crust: a global view. J. Geophys. Res. 100 (B6), 9761–9788. http://dx.doi.org/10.1029/95JB00259.

Chu, R., Helmberger, D.V., Sun, D., Jackson, J.M., Zhu, L., 2010. Mushy magma beneath Yellowstone. Geophys. Res. Lett. 37 (1), L01306. http://dx.doi.org/10.1029/2009GL041656.

Díaz, D., Heise, W., Zamudio, F., in press. 3-D resistivity image of the magmatic system beneath Lastarria volcano and evidence for magmatic intrusion in the back arc (Northern Chile). Geophys. Res. Lett.

Dziewonski, A., Bloch, S., Landisman, M., 1969. A technique for the analysis of transient seismic signals. Bull. Seismol. Soc. Am. 59 (1), 427–444.

Dzurisin, D., 2006. Volcano Deformation: New Geodetic Monitoring Techniques. Springer Science & Business Media.

Fournier, T.J., Pritchard, M.E., Riddick, S.N., 2010. Duration, magnitude, and frequency of subaerial volcano deformation events: new results from Latin America using InSAR and a global synthesis. Geochem. Geophys. Geosyst. 11, Q01003. http://dx.doi.org/10.1029/2009GC002558.

Froger, J.-L., Remy, D., Bonvalot, S., Legrand, D., 2007. Two scales of inflation at Lastarria–Cordon del Azufre volcanic complex, central Andes, revealed from ASAR-ENVISAT interferometric data. Earth Planet. Sci. Lett. 255 (1–2), 148–163. http://dx.doi.org/10.1016/j.epsl.2006.12.012.

Heimann, S., Trabs, S., Dahm, T., 2013. Lazufre volcanic complex, Chile: attempts to image a large-scale magmatic inflation body using regional and teleseismic broadband recordings. In: EGU General Assembly Conference Abstracts, p. 13072.

Henderson, S.T., Pritchard, M.E., 2013. Decadal volcanic deformation in the Central Andes Volcanic Zone revealed by InSAR time series. Geochem. Geophys. Geosyst. 14 (5), 1358–1374. http://dx.doi.org/10.1002/ggge.20074.

Iglesias, A., Cruz-Atienza, V.M., Shapiro, N.M., Singh, S.K., Pacheco, J.F., 2001. Crustal structure of south-central Mexico estimated from the inversion of surface-wave dispersion curves using genetic and simulated annealing algorithms. Geofís. Int. 40 (3), 181–190.

Ingebritsen, S.E., Sorey, M.L., 1985. A quantitative analysis of the Lassen hydrothermal system, North Central California. Water Resour. Res. 21 (6), 853–868. http://dx.doi.org/10.1029/WR021i006p00853.

Jay, J.A., Pritchard, M.E., West, M.E., Christensen, D., Haney, M., Minaya, E., Sunagua, M., McNutt, S.R., Zabala, M., 2012. Shallow seismicity, triggered seismicity, and ambient noise tomography at the long-dormant Uturuncu Volcano, Bolivia. Bull. Volcanol. 74 (4), 817–837. http://dx.doi.org/10.1007/s00445-011-0568-7.

Jaxybulatov, K., Shapiro, N.M., Koulakov, I., Mordret, A., Landès, M., Sens-Schönfelder, C., 2014. A large magmatic sill complex beneath the Toba caldera. Science 346 (6209), 617–619. http://dx.doi.org/10.1126/science.1258582.

Lees, J.M., 2007. Seismic tomography of magmatic systems. J. Volcanol. Geotherm. Res. 167 (1–4), 37–56. http://dx.doi.org/10.1016/j.jvolgeores.2007.06.008.

Legrand, D., Calahorrano, A., Guillier, B., Rivera, L., Ruiz, M., Villagómez, D., Yepes, H., 2002. Stress tensor analysis of the 1998–1999 tectonic swarm of northern Quito related to the volcanic swarm of Guagua Pichincha volcano, Ecuador. Tectonophysics 344 (1–2), 15–36. http://dx.doi.org/10.1016/S0040-1951(01)00273-6.

Levshin, A.L., Yanocskaya, T.B., Lander, A.V., Bukchin, B.G., Barmin, M.P., Ratnikova, L.I., Its, E.N., 1989. Keilis-Borok, V.I. (Ed.). Seismic Surface Waves in a Laterally Inhomogeneous Earth. Springer, New York.

Lu, Z., Dzurisin, D., Biggs, J., Wicks Jr., C.W., McNutt, S.R., 2010. Ground surface deformation patterns, magma supply, and magma storage at Okmok volcano, Alaska, from InSAR analysis: 1. Intereruption deformation, 1997–2008. J. Geophys. Res. 115, B00B02. http://dx.doi.org/10.1029/2009JB006969.

Marsh, B.D., 2000. Magma chambers. In: Encyclopedia of Volcanoes, pp. 191–206.

Masterlark, T., Haney, M., Dickinson, H., Fournier, T., Searcy, C., 2010. Rheologic and structural controls on the deformation of Okmok volcano, Alaska: FEMs, InSAR, and ambient noise tomography. J. Geophys. Res. 115 (B2), B02409. http://dx.doi.org/10.1029/2009JB006324.

Menke, W., 2012. Geophysical Data Analysis: Discrete Inverse Theory. Academic Press.

Mordret, A., Landès, M., Shapiro, N.M., Singh, S.C., Roux, P., Barkved, O.I., 2013. Near-surface study at the Valhall oil field from ambient noise surface wave tomography. Geophys. J. Int. http://dx.doi.org/10.1093/gji/ggt061.

Mordret, A., Rivet, D., Landès, M., Shapiro, N.M., 2014. 3-D shear-velocity anisotropic model of Piton de la Fournaise volcano (La Réunion Island) from ambient seismic noise. J. Geophys. Res., Solid Earth. http://dx.doi.org/10.1002/2014JB011654.

Nagaoka, Y., Nishida, K., Aoki, Y., Takeo, M., Ohminato, T., 2012. Seismic imaging of magma chamber beneath an active volcano. Earth Planet. Sci. Lett. 333, 1–8. http://dx.doi.org/10.1016/j.epsl.2012.03.034.

Naranjo, J.A., 1985. Sulphur flows at Lastarria volcano in the North Chilean Andes. Nature 313 (6005), 778–780. http://dx.doi.org/10.1038/313778a0.

Pearse, J., Lundgren, P., 2013. Source model of deformation at Lazufre volcanic center, central Andes, constrained by InSAR time series. Geophys. Res. Lett. 40 (6), 1059–1064. http://dx.doi.org/10.1002/grl.50276.

Pritchard, M.E., Simons, M., 2002. A satellite geodetic survey of large-scale deformation of volcanic centers in the central Andes. Nature 418 (6894), 167–171. http://dx.doi.org/10.1038/nature00872.

Pritchard, M.E., Simons, M., 2004. An InSAR-based survey of volcanic deformation in the southern Andes. Geophys. Res. Lett. 31 (15), L15610. http://dx.doi.org/10.1029/2004GL020545.

Rawlinson, N., Sambridge, M., 2004. Wave front evolution in strongly heterogeneous layered media using the fast marching method. Geophys. J. Int. 156 (3), 631–647. http://dx.doi.org/10.1111/j.1365-246X.2004.02153.x.

Rawlinson, N., Hauser, J., Sambridge, M., 2008. Seismic ray tracing and wavefront tracking in laterally heterogeneous media. Adv. Geophys. 49, 203–273. http://dx.doi.org/10.1016/S0065-2687(07)49003-3.

Remy, D., Froger, J.L., Perfettini, H., Bonvalot, S., Gabalda, G., Albino, F., Cayol, V., Legrand, D., Saint Blanquat, M.D., 2014. Persistent uplift of the Lazufre volcanic complex (Central Andes): new insights from PCAIM inversion of InSAR time series and GPS data. Geochem. Geophys. Geosyst. http://dx.doi.org/10.1002/2014GC005370.

Ruch, J., Anderssohn, J., Walter, T.R., Motagh, M., 2008. Caldera-scale inflation of the Lazufre volcanic area, South America: evidence from InSAR. J. Volcanol. Geotherm. Res. 174 (4), 337–344. http://dx.doi.org/10.1016/j.jvolgeores.2008.03.009.

Ruch, J., Manconi, A., Zeni, G., Solaro, G., Pepe, A., Shirzaei, M., Walter, T.R., Lanari, R., 2009. Stress transfer in the Lazufre volcanic area, central Andes. Geophys. Res. Lett. 36 (22), L22303. http://dx.doi.org/10.1029/2009GL041276.

Ruch, J., Walter, T.R., 2010. Relationship between the InSAR-measured uplift, the structural framework, and the present-day stress field at Lazufre volcanic area, central Andes. Tectonophysics 492 (1–4), 133–140. http://dx.doi.org/10.1016/j.tecto.2010.06.003.

Sabra, K.G., Gerstoft, P., Roux, P., Kuperman, W.A., Fehler, M.C., 2005. Extracting time-domain Green's function estimates from ambient seismic noise. Geophys. Res. Lett. 32 (3), L03310. http://dx.doi.org/10.1029/2004GL021862.

Sethian, J.A., 1996. A fast marching level set method for monotonically advancing fronts. Proc. Nat. Acad. Sci. 93 (4), 1591–1595. http://dx.doi.org/10.1073/pnas.93.4.1591.

Shapiro, N.M., Singh, S.K., 1999. A systematic error in estimating surface-wave group-velocity dispersion curves and a procedure for its correction. Bull. Seismol. Soc. Am. 89 (4), 1138–1142.

Shapiro, N.M., Campillo, M., 2004. Emergence of broadband Rayleigh waves from correlations of the ambient seismic noise. Geophys. Res. Lett. 31 (7). http://dx.doi.org/10.1029/2004GL019491.

Shapiro, N.M., Campillo, M., Stehly, L., Ritzwoller, M.H., 2005. High-resolution surface-wave tomography from ambient seismic noise. Science 307 (5715), 1615–1618. http://dx.doi.org/10.1126/science.1108339.

Spica, Z., Cruz-Atienza, V.M., Reyes-Alfaro, G., Legrand, D., Iglesias, A., 2014. Crustal imaging of western Michoacán and the Jalisco Block, Mexico, from Ambient Seismic Noise. J. Volcanol. Geotherm. Res. 289, 193–201. http://dx.doi.org/10.1016/j.jvolgeores.2014.11.005.

Tamburello, G., Hansteen, T.H., Bredemeyer, S., Aiuppa, A., Tassi, F., 2014. Gas emissions from five volcanoes in northern Chile and implications for the volatiles budget of the Central Volcanic Zone. Geophys. Res. Lett. 41 (14). http://dx.doi.org/10.1002/2014GL060653.

Walter, Th.R., Motagh, M., 2014. Deflation and inflation of a large magma body beneath Uturuncu volcano, Bolivia? Insights from InSAR data, surface lineaments and stress modeling. Geophys. J. Int. http://dx.doi.org/10.1093/gji/ggu080.

Ward, K.M., Porter, R.C., Zandt, G., Beck, S.L., Wagner, L.S., Minaya, E., Tavera, H., 2013. Ambient noise tomography across the Central Andes. Geophys. J. Int. http://dx.doi.org/10.1093/gji/ggt166.

Ward, K.M., Zandt, G., Beck, S.L., Christensen, D.H., McFarlin, H., 2014. Seismic imaging of the magmatic underpinnings beneath the Altiplano–Puna volcanic complex from the joint inversion of surface wave dispersion and receiver functions. Earth Planet. Sci. Lett. 404, 43–53. http://dx.doi.org/10.1016/j.epsl.2014.07.022.

Wicks Jr., C.W., Dzurisin, D., Ingebritsen, S., Thatcher, W., Lu, Z., Iverson, J., 2002. Magmatic activity beneath the quiescent Three Sisters volcanic center, central Oregon Cascade Range, USA. Geophys. Res. Lett. 29 (7), 1122. http://dx.doi.org/10.1029/2001GL014205.